

Coherent Acoustic Control of Defect Orbital States in the Strong-Driving Limit

B.A. McCullian¹, V. Sharma¹, H.Y. Chen,³ J.C. Crossman¹, E.J. Mueller^{1,2}, and G.D. Fuchs^{1,4,*}

¹*School of Applied and Engineering Physics, Cornell University, Ithaca, New York 14853, USA*

²*Laboratory of Atomic and Solid State Physics, Cornell University, Ithaca, New York 14853, USA*

³*Department of Physics, Cornell University, Ithaca, New York 14853, USA*

⁴*Kavli Institute at Cornell for Nanoscale Science, Ithaca, New York 14853, USA*



(Received 16 March 2024; accepted 29 July 2024; published 19 August 2024)

We use a bulk acoustic wave resonator to demonstrate coherent control of the excited orbital states in a diamond nitrogen-vacancy (NV) center at cryogenic temperature. Coherent quantum control is an essential tool for understanding and mitigating decoherence. Moreover, characterizing and controlling orbital states is a central challenge for quantum networking, where optical coherence is tied to orbital coherence. We study resonant multiphonon orbital Rabi oscillations in both the frequency and time domain, extracting the strength of the orbital-phonon interactions and the coherence of the acoustically driven orbital states. We reach the strong-driving limit, where the physics is dominated by the coupling induced by the acoustic waves. We find agreement between our measurements, quantum master-equation simulations, and a Landau-Zener transition model in the strong-driving limit. Using perturbation theory, we derive an expression for the orbital Rabi frequency versus the acoustic drive strength that is nonperturbative in the drive strength and agrees well with our measurements for all acoustic powers. Motivated by continuous-wave spin-resonance-based decoherence protection schemes, we model the orbital decoherence and find good agreement between our model and our measured few-to-several-nanoseconds orbital decoherence times. We discuss the outlook for orbital decoherence protection.

DOI: 10.1103/PRXQuantum.5.030336

I. INTRODUCTION

Quantum coherent control strategies can be used to both study and mitigate decoherence. This idea, along with the associated opportunities for quantum technologies, has spurred the development of high-fidelity quantum control over superconducting [1], atomic [2], and quantum dot [3] systems, among many others. Coherent control of solid-state defect spins has enabled the development of decoherence protection schemes [4–8] that can aid in precision sensing [9,10] and quantum networking [11–19]. Here, we use an acoustic wave resonator at cryogenic temperature to demonstrate coherent control of the excited orbital states in a diamond nitrogen-vacancy (NV) center in the strong-driving limit and we explore orbital resonance-based decoherence mitigation.

Strain and electric fields can couple to the orbital states of a defect, limiting quantum coherence while also creating opportunities for coherent control. On the negative side, electric field fluctuations from nearby charge traps provide the leading source of spectral diffusion in NV centers [20], which is problematic for quantum networking applications that rely on frequency-matched photon emission. On the positive side, both static electric fields [21,22] and quasistatic strains [23] have been used to tune NV-center optical transitions. Dynamical strains can also be used for quantum control: they can be combined with optical pulses to generate coherent Raman sidebands [24,25] and manipulate spin [26]. Two recent results in other defects demonstrate the use of orbital interactions for quantum control. In the first, researchers have used the strong strain-orbit interaction in silicon-vacancy (SiV) defects in diamond to achieve spin control via dynamic strain [27]. In the second, researchers have used electric fields to control a combined orbital-spin ground-state transition in the neutrally charged NV center [28]. Given that mitigating spectral diffusion remains an ongoing challenge for using NV centers as quantum networking nodes and that coherent control can often be leveraged for decoherence protection, we can naturally ask: can

*Contact author: gdf9@cornell.edu

Published by the American Physical Society under the terms of the [Creative Commons Attribution 4.0 International license](#). Further distribution of this work must maintain attribution to the author(s) and the published article's title, journal citation, and DOI.

coherent orbital control protect NV centers against spectral diffusion?

In this work, we demonstrate coherent control within the negatively charged NV-center excited-state orbital-doublet manifold using gigahertz-frequency acoustic waves. We study the resulting coherent dynamics of the associated optical transitions. We observe orbital Rabi oscillations driven by a resonant multiphonon mechanism and quantify the coherence of the orbital states under acoustic drive. The orbital Rabi oscillations are well described by a strong-driving Hamiltonian [29,30] and the Rabi frequency measured in the time domain is consistent with the spectroscopic splitting of the optical transitions in the frequency domain. We numerically verify that our simple Hamiltonian model produces these same dynamics using quantum master-equation simulations and we analytically describe them using a direct calculation of the orbital Rabi frequency with both a Landau-Zener transfer matrix approach as well as a perturbative approach in the Floquet picture. We characterize the coherence of the acoustically driven orbital states, finding at least a factor-of-2 enhancement of the coherence time. Finally, we discuss orbital-coherence enhancement by making an analogy with continuous-wave spin dynamical decoupling.

II. STRAIN-ORBITAL AND ACOUSTIC ORBITAL INTERACTIONS

We probe the acoustic driving of the excited-state orbital doublet using a tunable laser that is resonant with the spin-preserving zero-phonon optical transitions. These transitions couple the orbital-singlet spin-triplet (3A_2) ground states $\{|0\rangle, |\pm 1\rangle\}$ to orbital-doublet spin-triplet (3E) excited states $\{|E_{1,2}\rangle, |E_{x,y}\rangle, |A_{1,2}\rangle\}$ at around 1.945 eV (637.2 nm) [31], as shown in Fig. 1(d). Given that the transitions do not flip the spin state, it suffices to consider the $m_s = 0$ states. An unstrained NV center has C_{3v} point-group symmetry and degenerate $|0\rangle \leftrightarrow |E_{x,y}\rangle$ transition energies. The linear polarization of the laser can be rotated to selectively address the orthogonal transition dipoles that link the $m_s = 0$ ground and excited states, as shown by the red and blue arrows in Fig. 1(a). Persistent static strain in the diamond lifts this degeneracy. In the basis $\{|E_x\rangle, |E_y\rangle\}$, the interaction of the orbital excited states with static strain is given by

$$H = V_{A_1} \mathbb{1} + V_{E_1} \sigma_z + V_{E_2} \sigma_x, \quad (1)$$

where $\mathbb{1}$, σ_z , and σ_x are the identity matrix and the z and x Pauli matrices, respectively. The V_λ are strain-deformation potentials of Jahn-Teller [32] symmetry λ .

We generate the acoustic control field using a high-overtone bulk-mode acoustic resonator (HBAR) fabricated from single-crystal diamond [33], shown schematically in Fig. 1(a) (for fabrication details, see the Supplemental Material [34]). Gigahertz-frequency electrical driving

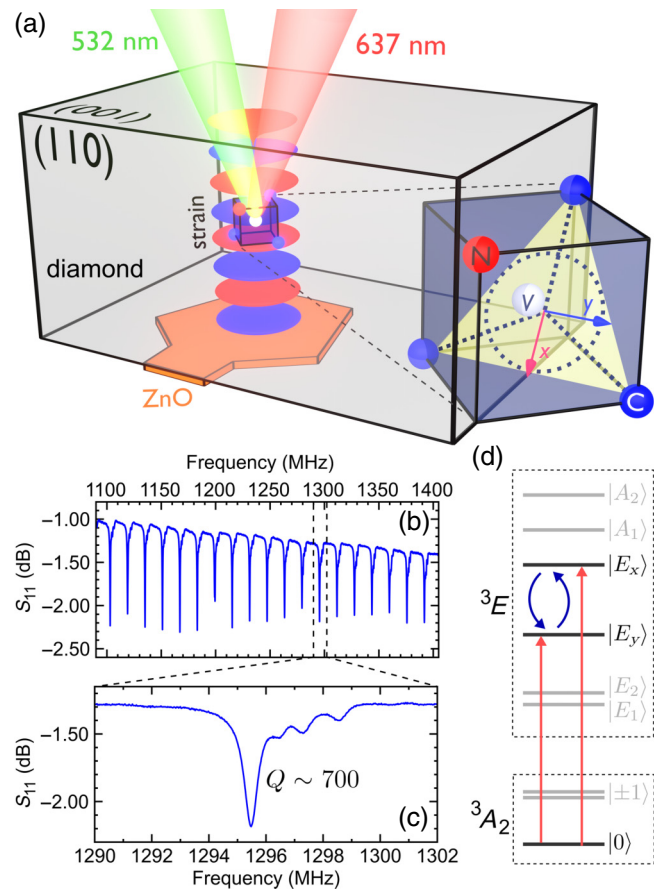


FIG. 1. A bulk acoustic wave resonator on diamond for acoustic orbital control. (a) A ZnO transducer (orange) excites the diamond (gray) high-overtone bulk-mode acoustic resonator (HBAR) with gigahertz-frequency uniaxial σ_{zz} -strain standing waves throughout the diamond bulk (red and blue lobes). A single bulk NV center (blue unit cell) is optically excited and fluorescence is collected through the diamond surface opposite the ZnO transducer. Dipoles x (red arrow) and y (blue arrow), corresponding to the $|0\rangle \leftrightarrow |E_x\rangle$ and $|0\rangle \leftrightarrow |E_y\rangle$ transitions, lie in a plane (yellow) normal to the NV-center C_{3v} symmetry axis. (b) S_{11} measurement of the electromechanical response of the HBAR device measured at room temperature. (c) The quality factor of the mode used for experiments is about 700. (d) The energy-level manifold for an NV center at low temperature. A resonant laser (red arrows) excites spin-preserving optical transitions, while acoustic driving (blue arrows) couples the orbital excited states.

of the HBAR at one of the resonance modes shown in Figs. 1(b) and 1(c) results in a standing longitudinal strain wave between the [001] diamond surfaces, which act as acoustic mirrors. The dynamic uniaxial strain introduces time-dependent terms into the Hamiltonian [25]:

$$H(t) = (V_{A_1} + \mathcal{A}_1 \cos(\omega_m t)) \mathbb{1} + (V_{E_1} + \mathcal{E}_1 \cos(\omega_m t)) \sigma_z + V_{E_2} \sigma_x, \quad (2)$$

where \mathcal{A}_1 (\mathcal{E}_1) is the dynamic strain driving amplitude of A_1 (E_1) symmetry and ω_m is the acoustic drive frequency. The geometry of our HBAR and NV center produces no dynamic E_2 -symmetric potential. The acoustic drive frequency for all our experiments is $\omega_m = 2\pi \times 1.296$ GHz.

III. ACOUSTICALLY DRIVEN ORBITAL STATES: FREQUENCY DOMAIN

We begin by measuring the zero-phonon-line optical transitions of a single bulk NV center using photoluminescence-excitation (PLE) spectroscopy [38] (for experimental details, see the Supplemental Material [34]). All photoluminescence measurements are taken at zero applied magnetic field and at a temperature of 7 K. We tune a resonant laser across the two $m_s = 0$ transition frequencies with the polarization set to excite both transitions equally while collecting the phonon sideband emission. We observe two peaks corresponding to the $|0\rangle \leftrightarrow |E_{x,y}\rangle$ transition frequencies [Fig. 2(a)] due to frequent reinitialization of the ground-state spin of the defect to $|0\rangle$ [23].

We then perform the same measurement in the presence of acoustic driving (0.63 mW to the transducer) and observe the emergence of coherent Raman sideband transitions at detunings of $\pm n\omega_m$ with respect to the undriven resonance frequencies [24,25]. The sidebands result from \mathcal{A}_1 modulation, allowing for optical transitions when the energy of one laser photon $\pm n$ acoustic phonons matches the undriven transition energies [39]. The sidebands are resolved since ω_m exceeds the line width of the optical transitions of the defect. We perform these measurements on several NV centers until we find one with an undriven $|E_x\rangle \leftrightarrow |E_y\rangle$ splitting that is an integer multiple of the standing wave generated by our acoustic drive.

Matching a multiple of our acoustic drive frequency to the strain splitting of the defect allows us to resonantly couple the orbital states. The acoustic modes of our HBAR have a spacing (16 MHz) set primarily by the thickness (500 μ m) of the diamond substrate. The acoustic mode spacing is considerably smaller than the line width of the optical transitions of the defects in the diamond (approx 100 MHz). Thus, we can select an acoustic mode for which an integer multiple of the acoustic driving frequency will match the orbital transition frequency. The splitting between $|E_x\rangle$ and $|E_y\rangle$ for the defect shown in Fig. 2 is $\Delta = 2\sqrt{V_{E_1}^2 + V_{E_2}^2} = 6.41$ GHz and $\Delta \approx 5\omega_m$. Our spectroscopy measurements provide a readout of the coupling strength. As we increase the acoustic drive power, we observe splitting of the PLE lines caused by resonant n -phonon driving of the $|E_x\rangle \leftrightarrow |E_y\rangle$ orbital transition [Fig. 2(b)]. This Autler-Townes splitting is the spectral signature of orbital Rabi oscillation and the line splitting gives

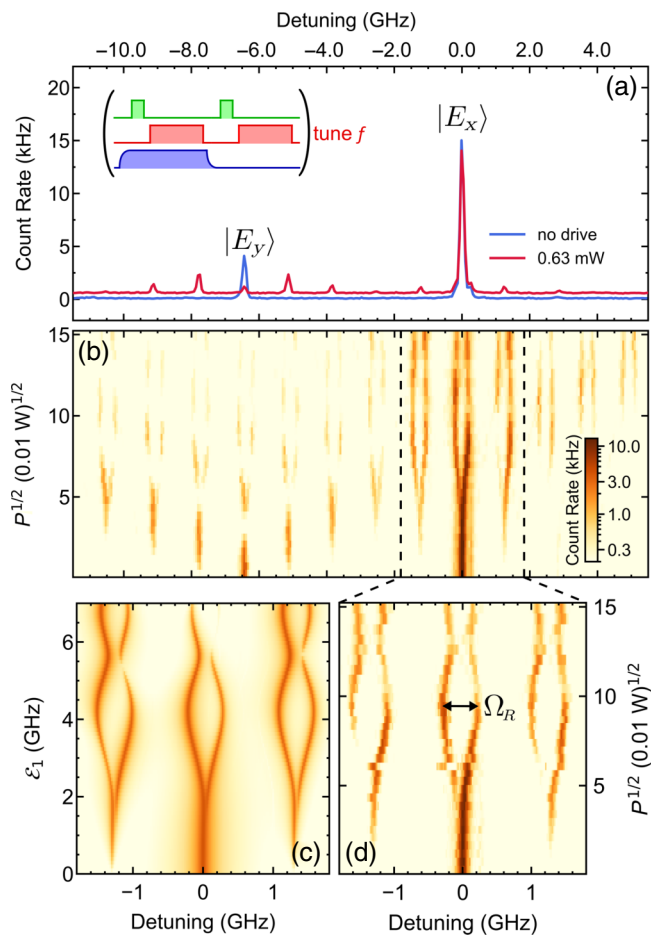


FIG. 2. Acoustically driven photoluminescence-excitation (PLE) spectroscopy. (a) PLE-spectroscopy measurements with the laser polarization set to couple to both orbital transitions, collected with no acoustic drive (blue trace) and weak acoustic drive (red trace), showing the emergence of resolved sideband transitions. The inset shows the sequence used for PLE-spectroscopy measurements: 1- μ s green laser, 5- μ s red laser and readout, 7- μ s acoustic drive, 500-ms collection at each red-laser frequency. (b) Acoustic power dependent PLE spectroscopy with the laser frequency swept across both $|E_{x,y}\rangle$ reveals sideband evolution and the emergence of Autler-Townes splitting. (c) Simulated spectroscopy near the undriven $|0\rangle \leftrightarrow |E_x\rangle$ transition frequency is in good agreement with (d) higher resolution spectroscopy measurements. As depicted in (d), the orbital Rabi rate Ω_R can be read off as a mode splitting. The acoustic mode frequency ω_m is $2\pi \times 1.296$ GHz and the splitting between $|E_x\rangle$ and $|E_y\rangle$ is $\Delta = 6.41$ GHz.

the Rabi-oscillation frequency Ω_R . This oscillation originates from the \mathcal{E}_1 driving in the presence of a nonzero V_{E_2} [25]. In a dressed-state picture, it is interpreted as a resonant multiphonon transition between the states $|E_x, m\rangle$ and $|E_y, m+5\rangle$, where m is the number of phonons dressing the optical transition.

We characterize the strength of the acoustic drive by comparing the spectroscopic splitting with simulation. We

collect a series of acoustic power dependent PLE scans in the vicinity of the undriven $|E_x\rangle$ frequency in Fig. 2(d). For each acoustic power, we fit the peak locations of the split spectrum and extract Ω_R . We find agreement between the measured spectrum and quantum master-equation simulations of the acoustically driven PLE spectrum [Fig. 2(c)] using the QuTiP PYTHON software [40] (see the Supplemental Material [34]) for the Hamiltonian given in Eq. (2). Thus, we can convert the applied acoustic drive power into a dynamic strain potential in units of gigahertz.

IV. ACOUSTICALLY DRIVEN ORBITAL STATES: TIME DOMAIN

We also study orbital Rabi oscillations in the time domain, which allows us to directly characterize Rabi frequencies and associated coherences. The orbital Rabi frequencies measured in Fig. 2(c) correspond to oscillation periods of a few nanoseconds, which is sufficiently fast that several oscillations will occur during the 12-ns excited-state lifetime [41,42]. Our scheme for measuring time-domain orbital Rabi oscillations is given in Fig. 3(a). We create an excited-state population primarily in the orbital state $|E_x\rangle$ by setting the laser frequency resonant to the $|0\rangle \leftrightarrow |E_x, m\rangle$ transition and setting the polarization to minimize coupling into $|E_y, m+5\rangle$. We resonantly excite the NV center with intense 1-ns-duration optical pulses that populate the excited state in a time that is shorter than the orbital dynamics. Given the fact that the acoustic drive is always on, longer pulses would be unable to selectively populate only one orbital state. Separate optical Rabi-oscillation measurements with the laser tuned to the $|0\rangle \leftrightarrow |E_x\rangle$ transition without acoustic driving confirm that we achieve a significant excited-state population with a 1-ns-long optical pulse (see the Supplemental Material [34]).

Time-domain measurements of acoustically driven orbital Rabi oscillations are shown in Figs. 3(b)–3(d). We record a histogram of photon arrivals relative to the onset of the excitation pulses for various acoustic drive powers. We observe a roughly exponential decay of photoluminescence as the defect undergoes spontaneous emission to the ground state. Dividing out the spontaneous emission response leaves us with an oscillatory residual, shown in Figs. 3(e)–3(g) as a percentage of the photoluminescence (PL) rate, which allows us to measure the orbital oscillations out to longer time scales than the spontaneous emission lifetime. We attribute the visibility of these oscillations to imperfect emission polarization selection rules of the two optical transitions and the efficiency with which photons emitted from each orbital branch exit the diamond and couple to our photon detector [20,43]. Thus, these residuals represent a direct time-domain measurement of the orbital Rabi oscillations. We fit the residuals to a decaying sinusoid of the form $y(t) = A \cos(\Omega_R t) e^{-t/T_{2,\text{Rabi}}}$ to

determine Ω_R and the orbital Rabi-coherence time $T_{2,\text{Rabi}}$. We observe a nonmonotonic evolution of Ω_R with acoustic drive power that matches the behavior found in spectroscopy. The full set of time-domain measurements and residuals is given in the Supplemental Material [34].

V. PERTURBATIVE EXPANSION IN V_{E_2}

The particular NV center in our experiment has $V_{E_2} \ll V_{E_1}$, which, as detailed in the Supplemental Material [34], allows us to derive a simple model for the E_{xy} manifold, including an expression for Ω_R , which is nonperturbative in the drive strength.

The crux of the calculation involves transforming to a rotating frame and introducing a Floquet ansatz. Second-order perturbation theory in V_{E_2} then maps the dynamics onto an undriven two-level system,

$$i\partial_t \begin{pmatrix} u_0 \\ v_0 \end{pmatrix} = \begin{pmatrix} \delta & \Omega_0 \\ \Omega_0 & -\delta \end{pmatrix} \begin{pmatrix} u_0 \\ v_0 \end{pmatrix}. \quad (3)$$

Here, u_0 and v_0 are the dominant frequency components of the Floquet wave function. Up to small corrections, $|u_0|^2$ and $|v_0|^2$ correspond to the probabilities of being in the $|E_x\rangle$ and $|E_y\rangle$ state. The parameters are

$$\delta = V_{E_1} - \frac{n\omega_m}{2} + \sum_{s \neq 0} \frac{|\Omega_s|^2}{s\omega_m}, \quad (4)$$

$$\Omega_s = V_{E_2} J_{s-n} \left(\frac{2\mathcal{E}_1}{\omega_m} \right), \quad (5)$$

where $J_s(x)$ is the Bessel function of order s . A special case of Eq. (5) is $\Omega_0 = V_{E_2} J_{-n}(2\mathcal{E}_1/\omega_m)$. At vanishing drive, $\delta(\mathcal{E}_1 = 0) = V_{E_1} - n\omega_m/2 + V_{E_2}^2/n\omega_m$ and $\Omega_0(\mathcal{E}_1 = 0) = 0$. At strong drive, $\delta(\mathcal{E}_1 \rightarrow \infty) = V_{E_1} - (n\omega_m)/2$ and $\Omega_0(\mathcal{E}_1 \rightarrow \infty) = 0$. Leading corrections are discussed in the Supplemental Material [34].

The Rabi frequency corresponds to the splitting between the eigenenergies of this equation,

$$\Omega_R = 2\sqrt{\delta^2 + \Omega_0^2}. \quad (6)$$

One can also consider dynamics. If we start at time $t = 0$ with the defect in the $|E_x\rangle$ state, the probability of being in the $|E_y\rangle$ state at time t is

$$P_y(t) = \frac{\Omega_0^2}{\Omega_0^2 + \delta^2} \sin^2 \Omega_R t / 2. \quad (7)$$

This expression is similar to Rabi's formula for the time dependence of a spin driven by a resonant microwave field [44]. Here, Ω_0 and δ play the role of the driving field and the detuning, respectively.

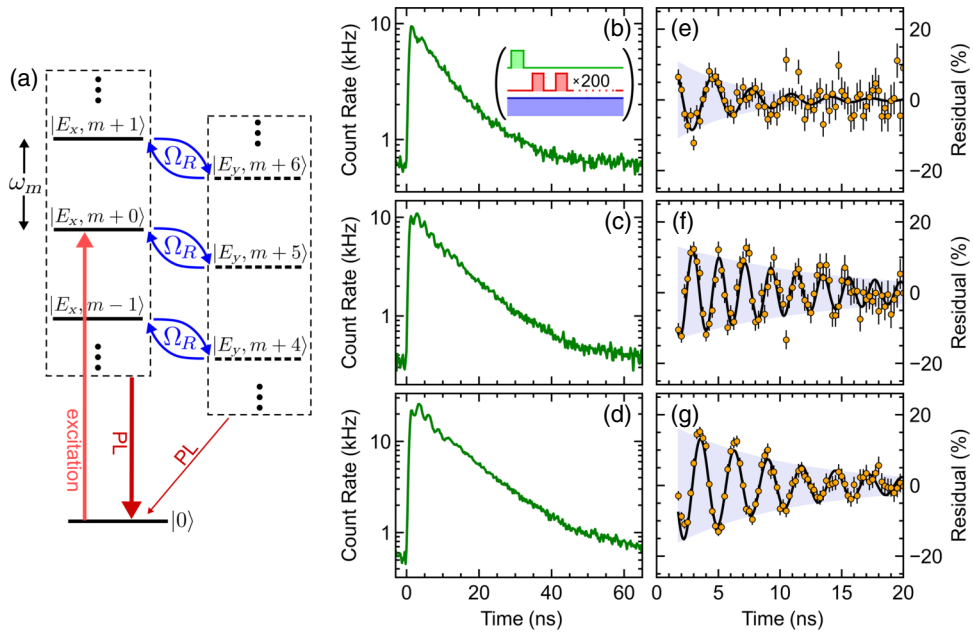


FIG. 3. Time-domain orbital Rabi oscillations. (a) The scheme for measuring orbital Rabi oscillations in the time domain. A 1-ns-duration excitation-laser pulse tuned resonantly to the undriven $|0\rangle \leftrightarrow |E_x, m + 0\rangle$ transition with polarization set to minimize coupling into $|E_y, m + 5\rangle$ excites into the $|E_x\rangle$ orbital manifold. Continuous-wave acoustic driving causes orbital Rabi oscillations between the $|E_x\rangle$ and $|E_y\rangle$ orbital states. The collected photoluminescence (PL) rate from $|E_x\rangle$ is larger than the rate from $|E_y\rangle$. (b)–(d) Histograms of time-tagged photon counts relative to the repeated 1-ns-duration red-laser pulses for acoustic drive powers P_m = (b) 14.5 mW, (c) 8.4 mW, and (d) 4.9 mW. The inset shows the pulse sequence: 2- μ s green laser, 200 repetitions of 1-ns red laser with 100 ns of delay between red pulses. Each histogram contains 2 min of collected counts. (e)–(g) Extracted residual oscillations for each acoustic power. Fits to decaying sinusoids (black trace) are used to extract the orbital Rabi frequency Ω_R and the orbital Rabi-coherence time $T_{2,\text{Rabi}}$: (e) $\Omega_R = 331 \pm 7$ MHz, $T_{2,\text{Rabi}} = 5.0 \pm 1.3$ ns; (f) $\Omega_R = 474 \pm 2$ MHz, $T_{2,\text{Rabi}} = 12.8 \pm 2.4$ ns; (g) $\Omega_R = 336 \pm 1$ MHz, $T_{2,\text{Rabi}} = 9.5 \pm 1.1$ ns. The error bars in (d)–(f) are determined assuming that the photon collection is shot-noise limited.

VI. ORBITAL RABI FREQUENCY AND COHERENCE

We compare the frequency and time-domain measurements of Ω_R versus the acoustic drive power. As shown in Fig. 4(a), they agree, confirming that our spectroscopy and time-domain measurements are probing the same effect. At small \mathcal{E}_1 , the Rabi splitting is largely insensitive to the drive— $\Delta \approx 5\omega_m$ —and hence one expects $\Omega_R \sim \mathcal{E}_1^5$ for small \mathcal{E}_1 . The Rabi splitting never exceeds 600 MHz, regardless of the drive strength. Physically, this corresponds to the fact that the orbital state cannot flip in a time that is shorter than half a period of the acoustic drive. This limitation is a consequence of the fact that the acoustic drive does not directly connect the orbital states but, instead, modulates their energies.

We take several approaches to model our experimental results. The most numerically exact of these is a quantum master-equation simulation of the frequency-domain response for a defect with the Hamiltonian given in Eq. (2) (see the Supplemental Material [34]). The blue-shaded region of Fig. 4(a) is the simulated range of Ω_R as we vary the acoustic drive power, assuming a 1% measurement error in the strain and optical-dipole orientation of

our defect. The data also agree very well with the second-order perturbation theory (SOPT) from Sec. V [black trace in Fig. 4(a)]. This perturbative approach is simpler than the master equation and gives some insight into the role being played by different components of the static strain. For example, the peaks and troughs are roughly located at the maxima and minima of $|\Omega_0|$ and the value of Ω_R at the minimum is set by δ .

Hamiltonians of the same form as Eq. (2) have been studied in a wide variety of contexts, including superconducting qubits [45], quantum dots [46], and NV-center spins [47,48], with particular interest in the strong-driving limit. In this limit, the amplitude of the drive $2\mathcal{E}_1$ is large compared to both the splitting Δ and the drive frequency ω_m and one can then interpret Eq. (2) as a periodic sequence of Landau-Zener (L.Z.) crossings. During one half-cycle, the coefficient of σ_z in Eq. (2) sweeps from a large positive value to a large negative value. As detailed in the Supplemental Material [34], one can approximate this with a linear sweep and derive analytic expressions for the orbital Rabi frequency [red trace in Fig. 4(a)], which are valid in the strong-drive limit, $\mathcal{E}_1 \gtrsim \Delta = 6.41$ GHz. This Landau-Zener model explains the oscillations observed in

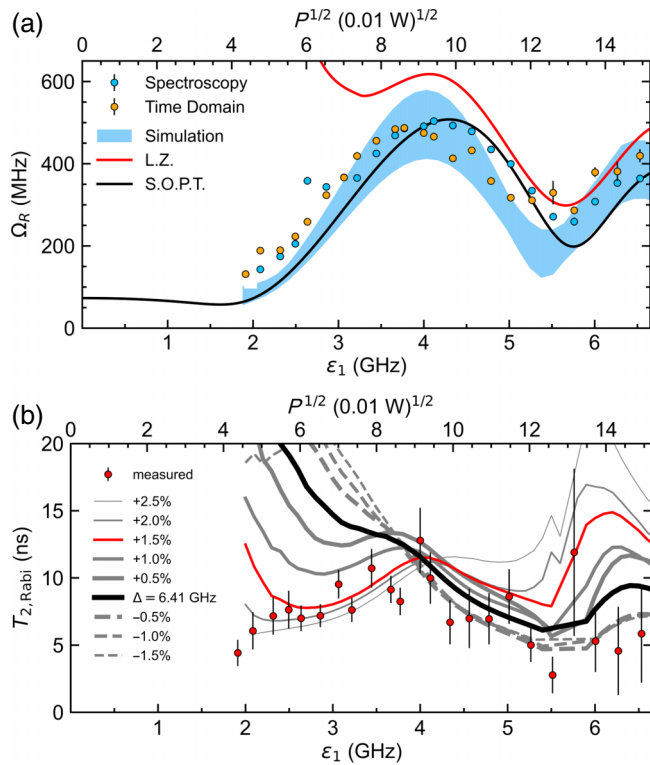


FIG. 4. The orbital Rabi-oscillation frequency and coherence. (a) Ω_R measured by spectroscopy (blue points) and in the time domain (orange points). The frequency-domain Lindblad simulation of Ω_R (blue-shaded region) for $\pm 1^\circ$ of uncertainty in defect dipole orientation and $\pm 1\%$ uncertainty in Δ . The second-order perturbation theory in V_{E_2} , given by Eq. (6) (black trace), is in good agreement with the measurement for the full range of drive amplitudes. The Landau-Zener transfer-matrix method (red trace) is a strong-drive approximation, valid at large \mathcal{E}_1 . (b) Measured $T_{2,\text{Rabi}}$ values (red points) extracted from the decay of acoustically driven orbital residual oscillations [Figs. 3(e)–3(g)]. The simulated decay time of the orbital coherence for 35-MHz standard deviation Gaussian-distributed electric field fluctuations (series of traces). The model has a strong dependence on Δ and the data are best described by using a value that is 1.5% above the nominal $\Delta = 6.41$ GHz, which is within our experimental error in measuring Δ .

Fig. 4(a) as interference terms coming from sequential crossings [29].

Measuring orbital Rabi oscillations in the time domain allows us to extract the orbital Rabi-coherence time $T_{2,\text{Rabi}}$ from the exponential decay of the time-domain residuals. We plot the extracted $T_{2,\text{Rabi}}$ versus Ω_R in Fig. 4(b). The orbital Rabi coherence decays on the few-to-several nanoseconds time scale, depending on the acoustic power. These time scales are similar to NV-center optical Ramsey coherence times that have been previously reported [49], suggesting a common origin. The coupling of our mechanical resonator to the orbital transition is sensitive to

fluctuations that detune the orbital splitting from the multiphonon acoustic drive frequency. Thus, the orbital Rabi coherence decays as a result of electric field fluctuations that are transverse to the NV-center symmetry axis [50]. Comparatively, optical Ramsey measurements are sensitive to fluctuations that change the ground-to-excited-state transition energy, which includes fluctuations both along and transverse to the NV-center symmetry axis.

The decay of orbital Rabi oscillations can be understood using a model based on Eq. (3). Here, we assume that orbital decoherence results from fluctuations in the electric field environment of the defect that modify the strain terms in Eqs. (4) and (5): $V_{E_1} \rightarrow V_{E_1} + \mathcal{E}_x$ and $V_{E_2} \rightarrow V_{E_2} + \mathcal{E}_y$. A common source of such fluctuations is shot-to-shot variation of the charge-trap environment of the defect caused by the 532-nm laser, the same fluctuations that are responsible for spectral diffusion [20]. We simulate the orbital Rabi decoherence by averaging an ensemble of sinusoidal quantum trajectories described by Eq. (7) with a random set of electric field fluctuations $\mathcal{E}_x, \mathcal{E}_y$ drawn from a Gaussian distribution with a 35-MHz width (see the Supplemental Material [34]). Though the lifetime of diamond charge traps can be of order 10 ms under no illumination [51], our application of about 10^7 charge repump pulses causes frequent change in the charge-state environment. We record fewer than one photon per charge repump and thus assume that the charge-trap-environment fluctuations are uncorrelated in our coherence simulations. As shown in Fig. 4(b), the result is quite sensitive to the splitting Δ . For $\mathcal{E}_1 < 6$ GHz, we find reasonable agreement with our measurements if we increase Δ by 1.5% from its nominal value of 6.41 GHz. This deviation is within the experimental uncertainty of our spectroscopic measurement of Δ . At our largest drive strengths, the decay time seems to be better fitted by a model where Δ is a fraction of a percent below its nominal value. This discrepancy could potentially be resolved by using a more sophisticated model for the electric field fluctuations or by including further decoherence mechanisms.

VII. CONCLUSIONS AND OUTLOOK

Previously, we have proposed the use of acoustic driving to engineer optical transition frequencies that are protected against transverse electric field noise [25]. Additionally, our prior work indicates that many bulk NV centers are dominated by spectral-diffusion sources transverse to the defect symmetry axis [50]. Together, these results suggest that orbital driving can mitigate spectral diffusion for some NV centers. Measuring orbital Rabi oscillations in the time domain is an essential first step toward such a decoherence protection scheme.

In the current study, we find modest decoherence protection. The decoherence time is a nonmonotonic function of the drive strength and for this defect can be enhanced by at

least a factor of 2. The model in Sec. V lets us understand this nonmonotonic behavior by making an analogy with the physics of a spin in a magnetic field under continuous microwave driving. For such a spin system, increasing the drive amplitude creates dressed states that are robust against magnetic field fluctuations, resulting in continuous-wave dynamical decoupling [5–7]. In Eq. (3), fluctuations of V_{E_1} are akin to magnetic field noise, shifting the detuning δ between the two states. Fluctuations of V_{E_2} play the role of both field- and amplitudelike noise, shifting both δ and the transition-matrix element, Ω_0 . As the acoustic drive power is varied, the decoherence is dominated by one or the other source of fluctuations. When Ω_R is large, the fluctuations of V_{E_2} dominate; and when Ω_R is small, fluctuations of V_{E_1} are most important. Thus, for this NV center, acoustic driving of the orbital states is limited to a modest improvement of the orbital coherence, since the two contributions to decoherence are not simultaneously negated.

Developing an orbital control scheme that mitigates all transverse fluctuations is possible by varying the device geometry. The bottleneck for our scheme is the reliance on a static V_{E_2} strain to couple the orbital states [Eq. (2)], which results in V_{E_2} fluctuations entering as amplitudelike noise in the decoherence process. Engineering a resonator-defect geometry that provides direct off-diagonal driving can result in a drive amplitude that is independent of the static strain terms, allowing for full decoherence mitigation. Additionally, electric field control of the orbital states [28,52] can be leveraged for pulsed orbital driving and to tune the orbital splitting [21,53]. Our acoustic orbital driving technique can be applied to any defect system with an orbital multiplet; e.g., some species of divacancies in silicon carbide that have the same orbital structure as the NV center in diamond [54]. Additionally, the group-IV split-vacancy defects in diamond have an orbital-doublet ground state [55–57] that can be manipulated acoustically. Overall, coherent orbital control will enable researchers to apply the robust toolbox of continuous-wave dynamical decoupling protocols to engineer dressed orbital states. Such dressed states can have coherent single-photon emission with improved frequency stability for defect-based quantum networking schemes.

ACKNOWLEDGMENTS

This work was supported by the Office of Naval Research under Grant No. N00014-21-1-2614 and by the National Science Foundation (NSF) under Grant No. PHY-2110250. The device fabrication was performed in part at the Cornell Nanoscale Facility, a member of the National Nanotechnology Coordinated Infrastructure (NNCI), which is supported by the NSF (Grant No. NNCI-2025233), and at the Cornell Center for Materials Research Shared Facilities, which are supported through

the NSF Materials Research Science and Engineering Centers (MRSEC) program (Grant No. DMR-1719875).

- [1] M. H. Devoret and R. J. Schoelkopf, Superconducting circuits for quantum information: An outlook, *Science* **339**, 1169 (2013).
- [2] M. Saffman, T. G. Walker, and K. Mølmer, Quantum information with Rydberg atoms, *Rev. Mod. Phys.* **82**, 2313 (2010).
- [3] R. Hanson, L. P. Kouwenhoven, J. R. Petta, S. Tarucha, and L. M. K. Vandersypen, Spins in few-electron quantum dots, *Rev. Mod. Phys.* **79**, 1217 (2007).
- [4] G. de Lange, Z. H. Wang, D. Ristè, V. V. Dobrovitski, and R. Hanson, Universal dynamical decoupling of a single solid-state spin from a spin bath, *Science* **330**, 60 (2010).
- [5] X. Xu, Z. Wang, C. Duan, P. Huang, P. Wang, Y. Wang, N. Xu, X. Kong, F. Shi, X. Rong, and J. Du, Coherence-protected quantum gate by continuous dynamical decoupling in diamond, *Phys. Rev. Lett.* **109**, 070502 (2012).
- [6] D. A. Golter, T. K. Baldwin, and H. Wang, Protecting a solid-state spin from decoherence using dressed spin states, *Phys. Rev. Lett.* **113**, 237601 (2014).
- [7] E. R. MacQuarrie, T. A. Gosavi, S. A. Bhave, and G. D. Fuchs, Continuous dynamical decoupling of a single diamond nitrogen-vacancy center spin with a mechanical resonator, *Phys. Rev. B* **92**, 224419 (2015).
- [8] C. P. Anderson, E. O. Glen, C. Zeledon, A. Bourassa, Y. Jin, Y. Zhu, C. Vorwerk, A. L. Crook, H. Abe, J. Ul-Hassan, T. Ohshima, N. T. Son, G. Galli, and D. D. Awschalom, Five-second coherence of a single spin with single-shot readout in silicon carbide, *Sci. Adv.* **8**, eabm5912 (2022).
- [9] J. M. Boss, K. S. Cujia, J. Zopes, and C. L. Degen, Quantum sensing with arbitrary frequency resolution, *Science* **356**, 837 (2017).
- [10] J. F. Barry, J. M. Schloss, E. Bauch, M. J. Turner, C. A. Hart, L. M. Pham, and R. L. Walsworth, Sensitivity optimization for NV-diamond magnetometry, *Rev. Mod. Phys.* **92**, 015004 (2020).
- [11] E. Togan, Y. Chu, A. S. Trifonov, L. Jiang, J. Maze, L. Childress, M. V. G. Dutt, A. S. Sørensen, P. R. Hemmer, A. S. Zibrov, and M. D. Lukin, Quantum entanglement between an optical photon and a solid-state spin qubit, *Nature* **466**, 730 (2010).
- [12] H. Bernien, L. Childress, L. Robledo, M. Markham, D. Twitchen, and R. Hanson, Two-photon quantum interference from separate nitrogen vacancy centers in diamond, *Phys. Rev. Lett.* **108**, 043604 (2012).
- [13] A. Sipahigil, M. L. Goldman, E. Togan, Y. Chu, M. Markham, D. J. Twitchen, A. S. Zibrov, A. Kubanek, and M. D. Lukin, Quantum interference of single photons from remote nitrogen-vacancy centers in diamond, *Phys. Rev. Lett.* **108**, 143601 (2012).
- [14] H. Bernien, B. Hensen, W. Pfaff, G. Koolstra, M. S. Blok, L. Robledo, T. H. Taminiau, M. Markham, D. J. Twitchen, L. Childress, and R. Hanson, Heralded entanglement between solid-state qubits separated by three metres, *Nature* **497**, 86 (2013).

- [15] W. Pfaff, B. J. Hensen, H. Bernien, S. B. van Dam, M. S. Blok, T. H. Taminiau, M. J. Tiggelman, R. N. Schouten, M. Markham, D. J. Twitchen, and R. Hanson, Unconditional quantum teleportation between distant solid-state quantum bits, *Science* **345**, 532 (2014).
- [16] S. Wehner, D. Elkouss, and R. Hanson, Quantum Internet: A vision for the road ahead, *Science* **362**, eaam9288 (2018).
- [17] D. D. Awschalom, R. Hanson, J. Wrachtrup, and B. B. Zhou, Quantum technologies with optically interfaced solid-state spins, *Nat. Photonics* **12**, 516 (2018).
- [18] M. Pompili, S. L. N. Hermans, S. Baier, H. K. C. Beukers, P. C. Humphreys, R. N. Schouten, R. F. L. Vermeulen, M. J. Tiggelman, L. dos Santos Martins, B. Dirkse, S. Wehner, and R. Hanson, Realization of a multinode quantum network of remote solid-state qubits, *Science* **372**, 259 (2021).
- [19] S. L. N. Hermans, M. Pompili, H. K. C. Beukers, S. Baier, J. Borregaard, and R. Hanson, Qubit teleportation between non-neighbouring nodes in a quantum network, *Nature* **605**, 663 (2022).
- [20] K.-M. C. Fu, C. Santori, P. E. Barclay, L. J. Rogers, N. B. Manson, and R. G. Beausoleil, Observation of the dynamic Jahn-Teller effect in the excited states of nitrogen-vacancy centers in diamond, *Phys. Rev. Lett.* **103**, 256404 (2009).
- [21] L. C. Bassett, F. J. Heremans, C. G. Yale, B. B. Buckley, and D. D. Awschalom, Electrical tuning of single nitrogen-vacancy center optical transitions enhanced by photoinduced fields, *Phys. Rev. Lett.* **107**, 266403 (2011).
- [22] V. M. Acosta, C. Santori, A. Faraon, Z. Huang, K.-M. C. Fu, A. Stacey, D. A. Simpson, K. Ganesan, S. Tomljenovic-Hanic, A. D. Greentree, S. Prawer, and R. G. Beausoleil, Dynamic stabilization of the optical resonances of single nitrogen-vacancy centers in diamond, *Phys. Rev. Lett.* **108**, 206401 (2012).
- [23] K. W. Lee, D. Lee, P. Ovartchaiyapong, J. Minguzzi, J. R. Maze, and A. C. Bleszynski Jayich, Strain coupling of a mechanical resonator to a single quantum emitter in diamond, *Phys. Rev. Appl.* **6**, 034005 (2016).
- [24] D. A. Golter, T. Oo, M. Amezcuá, K. A. Stewart, and H. Wang, Optomechanical quantum control of a nitrogen-vacancy center in diamond, *Phys. Rev. Lett.* **116**, 143602 (2016).
- [25] H. Y. Chen, E. R. MacQuarrie, and G. D. Fuchs, Orbital state manipulation of a diamond nitrogen-vacancy center using a mechanical resonator, *Phys. Rev. Lett.* **120**, 167401 (2018).
- [26] D. A. Golter, T. Oo, M. Amezcuá, I. Lekavicius, K. A. Stewart, and H. Wang, Coupling a surface acoustic wave to an electron spin in diamond via a dark state, *Phys. Rev. X* **6**, 041060 (2016).
- [27] S. Maity, L. Shao, S. Bogdanović, S. Meesala, Y.-I. Sohn, N. Sinclair, B. Pingault, M. Chalupnik, C. Chia, L. Zheng, K. Lai, and M. Lončar, Coherent acoustic control of a single silicon vacancy spin in diamond, *Nat. Commun.* **11**, 193 (2020).
- [28] H. Kurokawa, K. Wakamatsu, S. Nakazato, T. Makino, H. Kato, Y. Sekiguchi, and H. Kosaka, Coherent electric field control of orbital state of a neutral nitrogen-vacancy center, *Nat. Commun.* **15**, 4039 (2024).
- [29] S. Ashhab, J. R. Johansson, A. M. Zagoskin, and F. Nori, Two-level systems driven by large-amplitude fields, *Phys. Rev. A* **75**, 063414 (2007).
- [30] G. D. Fuchs, V. V. Dobrovitski, D. M. Toyli, F. J. Heremans, and D. D. Awschalom, Gigahertz dynamics of a strongly driven single quantum spin, *Science* **326**, 1520 (2009).
- [31] G. Davies and M. Hamer, Optical studies of the 1.945 eV vibronic band in diamond, *Proc. R. Soc. Lond. A Math. Phys. Sci.* **348**, 285 (1976).
- [32] H. A. Jahn and E. Teller, Stability of polyatomic molecules in degenerate electronic states—I—Orbital degeneracy, *Proc. R. Soc. Lond. A* **161**, 220 (1937).
- [33] E. R. MacQuarrie, T. A. Gosavi, N. R. Jungwirth, S. A. Bhave, and G. D. Fuchs, Mechanical spin control of nitrogen-vacancy centers in diamond, *Phys. Rev. Lett.* **111**, 227602 (2013).
- [34] See the Supplemental Material at <http://link.aps.org/supplemental/10.1103/PRXQuantum.5.030336> for details on fabrication, experimental methods, simulations, and theory, which includes Refs. [35–37].
- [35] N. Goldman and J. Dalibard, Periodically driven quantum systems: Effective Hamiltonians and engineered gauge fields, *Phys. Rev. X* **4**, 031027 (2014).
- [36] M. Rodriguez-Vega, M. Lentz, and B. Seradjeh, Floquet perturbation theory: Formalism and application to low-frequency limit, *New J. Phys.* **20**, 093022 (2018).
- [37] E. S. Mananga and T. Charpentier, Introduction of the Floquet-Magnus expansion in solid-state nuclear magnetic resonance spectroscopy, *J. Chem. Phys.* **135**, 044109 (2011).
- [38] F. Jelezko, I. Popa, A. Gruber, C. Tietz, J. Wrachtrup, A. Nizovtsev, and S. Kilin, Single spin states in a defect center resolved by optical spectroscopy, *Appl. Phys. Lett.* **81**, 2160 (2002).
- [39] A. Albrecht, A. Retzker, F. Jelezko, and M. B. Plenio, Coupling of nitrogen vacancy centres in nanodiamonds by means of phonons, *New J. Phys.* **15**, 083014 (2013).
- [40] J. Johansson, P. Nation, and F. Nori, QuTiP: An open-source PYTHON framework for the dynamics of open quantum systems, *Comput. Phys. Commun.* **183**, 1760 (2012).
- [41] A. Batalov, C. Zierl, T. Gaebel, P. Neumann, I.-Y. Chan, G. Balasubramanian, P. R. Hemmer, F. Jelezko, and J. Wrachtrup, Temporal coherence of photons emitted by single nitrogen-vacancy defect centers in diamond using optical Rabi-oscillations, *Phys. Rev. Lett.* **100**, 077401 (2008).
- [42] M. L. Goldman, A. Sipahigil, M. W. Doherty, N. Y. Yao, S. D. Bennett, M. Markham, D. J. Twitchen, N. B. Manson, A. Kubanek, and M. D. Lukin, Phonon-induced population dynamics and intersystem crossing in nitrogen-vacancy centers, *Phys. Rev. Lett.* **114**, 145502 (2015).
- [43] F. Kaiser, V. Jacques, A. Batalov, P. Siyushev, F. Jelezko, and J. Wrachtrup, Polarization properties of single photons emitted by nitrogen-vacancy defect in diamond at low temperature, *ArXiv:0906.3426*.
- [44] A. Abragam and B. Bleaney, *Electron paramagnetic resonance of transition ions* (Clarendon Press, Oxford, United Kingdom, 1970).
- [45] W. D. Oliver, Y. Yu, J. C. Lee, K. K. Berggren, L. S. Levitov, and T. P. Orlando, Mach-Zehnder interferometry in

- a strongly driven superconducting qubit, [Science 310, 1653 \(2005\)](#).
- [46] Y.-C. Yang, S. N. Coppersmith, and M. Friesen, High-fidelity single-qubit gates in a strongly driven quantum-dot hybrid qubit with 1/f charge noise, [Phys. Rev. A 100, 022337 \(2019\)](#).
- [47] L. Childress and J. McIntyre, Multifrequency spin resonance in diamond, [Phys. Rev. A 82, 033839 \(2010\)](#).
- [48] G. Wang, Y.-X. Liu, and P. Cappellaro, Observation of the high-order Mollow triplet by quantum mode control with concatenated continuous driving, [Phys. Rev. A 103, 022415 \(2021\)](#).
- [49] L. C. Bassett, F. J. Heremans, D. J. Christle, C. G. Yale, G. Burkard, B. B. Buckley, and D. D. Awschalom, Ultrafast optical control of orbital and spin dynamics in a solid-state defect, [Science 345, 1333 \(2014\)](#).
- [50] B. McCullian, H. Cheung, H. Chen, and G. Fuchs, Quantifying the spectral diffusion of N-V centers by symmetry, [Phys. Rev. Appl. 18, 064011 \(2022\)](#).
- [51] G. Wang, C. Li, H. Tang, B. Li, F. Madonini, F. F. Alsallom, W. K. C. Sun, P. Peng, F. Villa, J. Li, and P. Cappellaro, Manipulating solid-state spin concentration through charge transport, [Proc. Natl. Acad. Sci. 120, e2305621120 \(2023\)](#).
- [52] T. Delord, R. Monge, G. Lopez-Morales, O. Bach, C. E. Dreyer, J. Flick, and C. A. Meriles, Probing electric-dipole-enabled transitions in the excited state of the nitrogen-vacancy center in diamond, [ArXiv:2405.16280](#).
- [53] P. Tamarat, T. Gaebel, J. R. Rabeau, M. Khan, A. D. Greene, H. Wilson, L. C. L. Hollenberg, S. Prawer, P. Hemmer, F. Jelezko, and J. Wrachtrup, Stark shift control of single optical centers in diamond, [Phys. Rev. Lett. 97, 083002 \(2006\)](#).
- [54] D. J. Christle, P. V. Klimov, C. F. de las Casas, K. Szász, V. Ivády, V. Jokubavicius, J. Ul Hassan, M. Syväjärvi, W. F. Koehl, T. Ohshima, N. T. Son, E. Janzén, A. Gali, and D. D. Awschalom, Isolated spin qubits in SiC with a high-fidelity infrared spin-to-photon interface, [Phys. Rev. X 7, 021046 \(2017\)](#).
- [55] B. Machielse, S. Bogdanovic, S. Meesala, S. Gauthier, M. J. Burek, G. Joe, M. Chalupnik, Y. I. Sohn, J. Holzgrafe, R. E. Evans, C. Chia, H. Atikian, M. K. Bhaskar, D. D. Sukachev, L. Shao, S. Maity, M. D. Lukin, and M. Lončar, Quantum interference of electromechanically stabilized emitters in nanophotonic devices, [Phys. Rev. X 9, 031022 \(2019\)](#).
- [56] A. E. Rugar, C. Dory, S. Aghaeimeibodi, H. Lu, S. Sun, S. D. Mishra, Z.-X. Shen, N. A. Melosh, and J. Vučkové, Narrow-linewidth tin-vacancy centers in a diamond waveguide, [ACS Photonics 7, 2356 \(2020\)](#).
- [57] N. H. Wan, T.-J. Lu, K. C. Chen, M. P. Walsh, M. E. Trusheim, L. De Santis, E. A. Bersin, I. B. Harris, S. L. Mouradian, I. R. Christen, E. S. Bielejec, and D. Englund, Large-scale integration of artificial atoms in hybrid photonic circuits, [Nature 583, 226 \(2020\)](#).